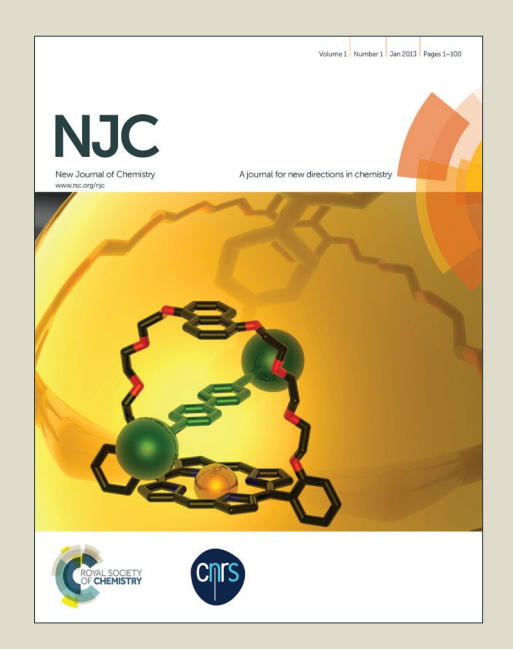
NJC

Accepted Manuscript



This is an *Accepted Manuscript*, which has been through the Royal Society of Chemistry peer review process and has been accepted for publication.

Accepted Manuscripts are published online shortly after acceptance, before technical editing, formatting and proof reading. Using this free service, authors can make their results available to the community, in citable form, before we publish the edited article. We will replace this Accepted Manuscript with the edited and formatted Advance Article as soon as it is available.

You can find more information about *Accepted Manuscripts* in the **Information for Authors**.

Please note that technical editing may introduce minor changes to the text and/or graphics, which may alter content. The journal's standard <u>Terms & Conditions</u> and the <u>Ethical guidelines</u> still apply. In no event shall the Royal Society of Chemistry be held responsible for any errors or omissions in this *Accepted Manuscript* or any consequences arising from the use of any information it contains.





Journal Name

ARTICLE

Received 00th January 20xx, Accepted 00th January 20xx

DOI: 10.1039/x0xx00000x

www.rsc.org/

One-pot solvothermal synthesis of bimetallic yolk-shell Ni@PtNi nanocrystals supported on reduced graphene oxide and their excellent catalytic properties for p-nitrophenol reduction

Li-Ping Mei, Rui Wang, Pei Song, Jiu-Ju Feng, Zhi-Gang Wang, Jian-Rong Chen, Ai-Jun Wang*

Well-defined bimetallic yolk-shell nanostructures of Ni@PtNi nanocrystals with porous shells were uniformly deposited on reduced graphene oxide (Ni@PtNi NCs-rGO) under hydrothermal conditions. The physical characterizations were systematically investigated by transmission electron microscopy, X-ray diffraction, and X-ray photoelectron spectroscopy. The as-fabricated products exhibited improved catalytic performance toward the reduction of ρ -nitrophenol in comparison to the commercial Pt/C (50 wt%), monometallic Pt nanoparticles/rGO and Ni nanoparticles/rGO catalysts.

1. Introduction

With the rapid development of chemical industry, there is a growing quantity of organic pollutants produced in pharmaceutics, leather, printing, paint and textile. As one of nitro compounds, p-nitrophenol (p-NP) in aqueous media is difficult to be biodegraded or self-cleaned, which causes a potential and prolonged toxic threat to amphibians and aquatic lives, even to human beings. As a result, many researchers have tried to solve this problem. For instance, the catalytic reduction of p-NP by metal-based catalysts was extensively investigated because of their brief operation, high efficiency, environment friendly, and relatively low cost.

Pt nanoparticles (NPs) with different size and shape are broadly employed as catalysts in organic reactions, ⁶ fuel cells, ⁸ and other applications. ^{9,10} To heighten the atomic utilization and sustainability, Pt-based bimetallic nanocatalysts are prepared, in which Pt is partially modified with another transition metals (i.e., Ni and Cu) as valid substitutions. Recent researches demonstrate their superior catalytic performances, possibly thanks to their unique geometric and electronic properties after the introduction of another metal. ^{11,12} For instance, Kim's group prepared Pt-Ni alloyed hollow nanoparticles with higher catalytic activity for oxygen reduction than commercial Pt/C catalyst. ¹³ Liu et al. fabricated porous Pt-Co alloy nanowires exhibiting markedly enhanced electrocatalytic activity toward methanol oxidation reaction (MOR) in contrast with commercial Pt/C. ¹⁴

However, large-scaled commercial applications of Pt-

based catalysts are seriously hindered because of their prone agglomeration during reuse. ¹⁵ Happily, these challenges can be efficiently solved by the employment of graphene materials as supporting materials. ¹⁶ Particularly, graphene oxide (GO) can be served as a promising carbon-based support to anchor metal catalysts, owing to its superior electrical conductivity, vitally large specific surface area, and preeminent chemical properties. ¹⁷ For example, Guo et al. fabricated bimetallic Pton-Pd nanodendrites on graphene sheets as an electrocatalyst for MOR. ¹⁸ Sahoo and co-workers synthesized RGO/Pt-Ni nanocatalysts, which showed superior catalytic performance for *p*-NP reduction as compared with bare Pt-Ni under the identical conditions. ⁵

It is well known that the catalytic activity of a catalyst was greatly determined by its shape, size, and composition. Yolkshell nanoparticles, as unique core/shell structures with a specific core/shell configuration, have attracted tremendous interest, owing to their enlarged surface area and low density. For example, Geng and co-workers synthesized Au-Pt yolk/shell nanostructure, which displayed an excellent Pt-based catalytic activity for MOR with notable CO-tolerance. 19

Herein, a facile and moderate one-pot approach was exploited for the fabrication of yolk-shell nanostructures of Ni@PtNi nanocrystals supported on reduced graphene oxide nanosheets (defined as Ni@PtNi NCs-rGO). They are directly prepared by heating the mixture of graphene oxide (GO), Pt(acac) $_2$ and Ni(acac) $_2$ in the presence of cetyltrimethylammonium chloride and n-butylamine for 10 h under solvothermal conditions.

2. Experimental section

2.1 Chemicals

Platinum acetylacetonate $(Pt(acac)_2)$ and nickel acetylacetonate $(Ni(acac)_2)$, N, N-dimethylformamide (DMF),

College of Geography and Environmental Science, College of Chemistry and Life Science, Zhejiang Normal University, Jinhua 321004, China.

E-mail: ajwang@zjnu.cn (A.J. Wang); Tel./Fax: +86 579 82282269.

Filectronic Sunnlementary Information (FSI) available: Experimental section

[†]Electronic Supplementary Information (ESI) available: Experimental section, synthetic procedures, XRD, Raman, TGA, XPS spectra.

See DOI: 10.1039/x0xx00000x

ARTICLE Journal Name

n-butylamine, graphite powder (8000 mesh), sodium borohydride (NaBH $_4$), p-nitrophenol (p-NP), commercial Pt/C (50 wt%), and cetyltrimethylammonium chloride (CTAC) were purchased from Shanghai Aladdin Chemical Reagent Company (Shanghai, China). All the other chemicals were of analytical grade and used as received.

2.1 Characterization

Transmission electron microscopy (TEM) and highresolution transmission electron microscopy (HR-TEM) images of the samples were obtained on JEM-2100F transmission electron microscope operating at 200 kV. The elemental composition analysis for the products was conducted by Energy-dispersive X-ray spectroscopy (EDS), and high-angle annular dark-field scanning transmission electron microscopy (HAADF-STEM) recorded on a JEM-2100F HR transmission electron microscope coupled with an energy-dispersive X-ray spectrometer (Oxford-1NCA). The composition and crystal structures were further investigated by X-ray diffraction (XRD) on a by Rigaku-D8-AXS diffractometer using a Cu-Kα radiation (Bruker Co., Germany). X-ray photoelectron spectroscopy (XPS) measurements were conducted on a K-Alpha XPS spectrometer (ThermoFisher, E. Grinstead, UK) with Al Kα Xray radiation (1486.6 eV) for excitation. Raman spectra were acquired on a Renishaw Raman system model 1000 spectrometer with the excitation from the 633 nm line of an Ar-ion laser. Thermo gravimetric analysis (TGA) was performed with a simultaneous thermo-gravimetric analyzer (NETZSCH STA 449C). The samples were heated from room temperature to 800 °C at a heat rate of 10 °C min⁻¹ in air atmosphere.

2.3 Preparation of Ni@PtNi NCs-rGO

Graphene oxide (GO) was firstly synthesized based on the modified Hummers' method. Then, 4.0 mg of Pt(acac)₂ and 7.7 mg of Ni(acac)₂ were dissolved into 3 mL of DMF, followed by the successive addition of 5 mL of GO (1.0 mg mL $^{-1}$), 10 mL of CTAC (0.01 M in DMF), and 1.5 mL of n-butylamine under stirring. After further stirring for 30 min, the resulting homogeneous mixture was transferred into a 25 mL Teflonlined autoclave and heated at 150 °C for 10 h, and cooled down to room temperature naturally. Purification of the black precipitates was based on the work previously. 21

For comparison, rGO supported Pt and Ni nanopaticles were also fabricated in a similar way, using single $Pt(acac)_2$ and $Ni(acac)_2$ as the precursors in control experiments, respectively, denoted as Pt NPs-rGO and Ni NPs-rGO.

2.4 Catalytic reduction of p-NP

Before the catalytic reduction of p-NP, the aqueous solutions of p-NP (1 mM) and NaBH₄ (0.5 M) were freshly prepared by mixing 0.5 mL of p-NP and 1 mL of NaBH₄ into 1 mL of water in the reaction cuvette. The catalytic reduction of p-NP was employed as a model system to examine the catalytic activity of the as-synthesized Ni@PtNi NCs-rGO.

The catalytic reaction was performed in a standard quartz cuvette at 298 K. After recording the UV-vis absorbance spectrum, the homogeneous suspension of Ni@PtNi NCs-rGO (1 mg mL⁻¹) was injected into the cuvette to trigger the catalytic reaction, followed by recording the time-dependent UV-vis spectra.

Control experiments were performed by replacing Ni@PtNi-rGO with commercial Pt/C (50 wt%), Pt NPs/rGO, and Ni NPs/rGO with the same concentrations for *p*-NP by varying the reaction temperature from 298 to 328 K.

3. Results and discussion

3.1 Characterization

As illustrated in Fig. 1A and B, the product contains a large number of well-dispersed yolk-shell nanostructures supported on rGO surface, with rough porous shells of 22 nm in thickness and yolks of 30 nm. The Ni@PtNi NCs have a very narrow size distribution from 59.5 to 83.5 nm with the average size of 72 nm (Fig. S1, Electronic Supplementary Information, ESI). HR-TEM images provide more detailed structural information of Ni@PtNi NCs (Fig. 1C). As shown in Fig. 1C (a and b), HR-TEM images are taken from the marked shell and core of Ni@PtNi NCs, respectively. The lattice spacing of 0.223 nm corresponds to the (111) crystal planes of PtNi (Fig. 1C, a), and the dspacing of 0.203 nm matches well with the \emph{d}_{111} of Ni phase (Fig. 1C, b). These results confirm good crystallization of the external PtNi shell and interior Ni core, as supported by the results from shell-core PtNi in the previous study. 11 Meanwhile, the use of GO is important to improve the dispersity of yolkshell Ni@PtNi NCs, but not vital for the formation of yolk-shell structures because similar structures are still obtained without GO in control experiments, albeit with their heavy aggregation (Fig. S2, ESI), revealing that the main role of GO is to protect and disperse Ni@PtNi NCs. The precise composition of yolkshell Ni@PtNi NCs was examined by inductively coupled plasma mass spectrometry (ICP-MS), the molar ratio of Pt to Ni was calculated to be 1:2.54. The result is similar to the Pt/Ni

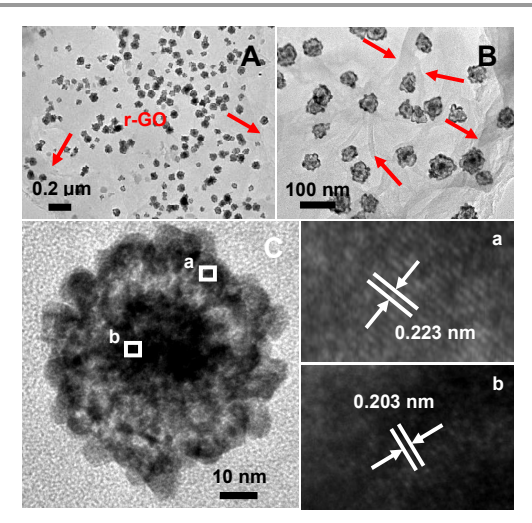


Fig. 1 (A) Low-, (B) middle-, and (C) HR-TEM images of Ni@PtNi NCs-rGO.

Journal Name ARTICLE

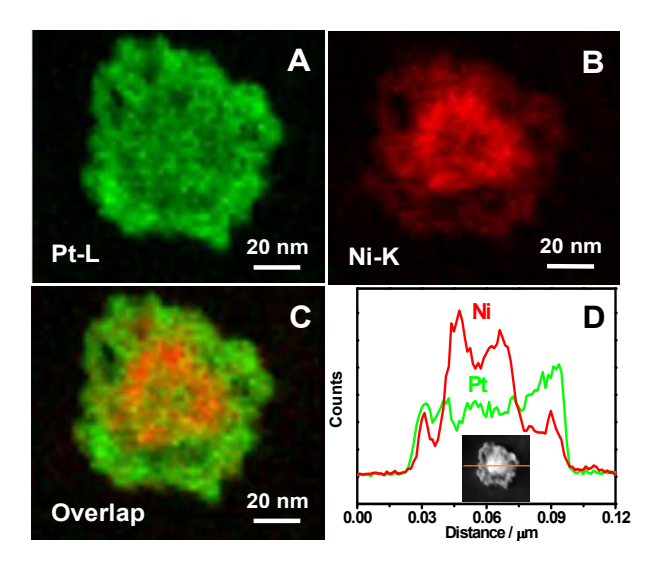


Fig. 2 (A-C) HAADF-STEM-EDS element mapping images and (D) line scanning profile of Ni@PtNi NCs-rGO.

molar ratio in the initial precursor solution (1:2.94), demonstrating the complete reduction of the Pt and Ni precursors.

Furthermore, the elemental distribution in Ni@PtNi NCs was determined by high-angle annular dark-field scanning transmission electron microscopy and energy-dispersive X-ray spectroscopy elemental mapping images (HAADF-STEM-EDS) and cross-sectional compositional line profiles (Fig. 2). As measured by EDS elemental mapping (Fig. 2A-C), Ni is mainly centred in the core, while Pt is distributed throughout the entire yolk-shell structure. These observations are in good accordance with the cross-sectional compositional line profiles of Pt and Ni elements (Fig. 2D), showing the formation of yolk-shell nanostructure. 22

Furthermore, the elemental distribution in Ni@PtNi NCs was determined by high-angle annular dark-field scanning transmission electron microscopy and energy-dispersive X-ray spectroscopy elemental mapping images (HAADF-STEM-EDS) and cross-sectional compositional line profiles (Fig. 2). As measured by EDS elemental mapping (Fig. 2A-C), Ni is mainly centred in the core, while Pt is distributed throughout the entire yolk-shell structure. These observations are in good accordance with the cross-sectional compositional line profiles of Pt and Ni elements (Fig. 2D), showing the formation of yolk-shell nanostructure. ²²

X-ray diffraction (XRD) pattern reveals the composition and crystal structure of Ni@PtNi NCs-rGO (Fig. 3A, curve a). The typical diffraction peaks at 40.0°, 46.5°, 67.9°, and 81.6° are assigned to the (111), (200), (220) and (311) planes of the face center cubic (fcc) of PtNi,²³ respectively, which reveals the presence of PtNi shell in Ni@PtNi NCs. However, these diffraction peaks are mildly deviated to higher 2θ values in contrast with bulk Pt (JCPDS NO. 04-0802), which is attributed to the shrinkage of the lattice due to the influence of Ni.²⁴ Moreover, the broaden peaks at 41.9°, 48.8° and a new peak

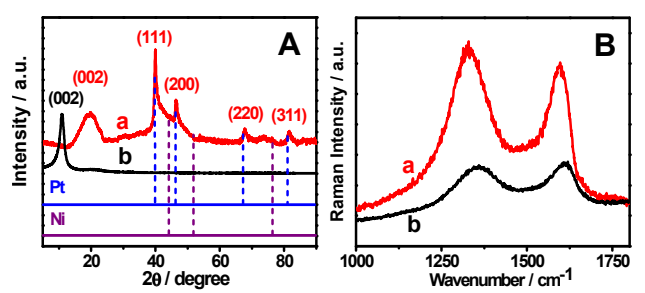


Fig. 3 (A) XRD patterns and (B) Raman spectra of Ni@PtNi NCs-rGO (curve a) and GO (curve b).

appearing at 73.9° are well indexed to the (111), (200), (220) planes of pure Ni (JCPDS NO. 04-0850), indicating the existence of Ni as a core. These results suggest that the yolk-shell nanostructures are composed of external PtNi shells and Ni cores, as the Ni core is generated first. This might be due to the decreased reduction potential of the Pt precursor in the presence of n-butylamine and CTAC, which can strong complex with the Pt precursor. Additionally, a broad diffraction peak around 19.4° can be detected for Ni@PtNi NCs-rGO, while the peak of bare GO (20 = 10.7°, Fig. 3A, curve b) has vanished, highlighting the efficient formation of rGO. These observations are identical with those in the literature.

The efficient reduction of GO is further confirmed by Raman spectroscopy (Fig. 3B). As for Ni@PtNi NCs-rGO (curve a), there are two main characteristic peaks located at around 1352 and 1595 cm⁻¹ corresponding to the D and G bands, ²⁷ respectively. Obviously, the two bands have slight blue shifts as compared with pure GO (curve b), thanks to the strong interactions between the yolk-shell nanostructures and graphene. ²⁸ The ratio of D to G peak intensity ($I_{\rm D}/I_{\rm G}$) is usually applied to calculate the disorder degree of graphite. ²⁹ The $I_{\rm D}/I_{\rm G}$ of Ni@PtNi NCs-rGO is 1.04, which is notably larger than that of bare GO (0.64), revealing that more defects are produced after the efficient reduction of exfoliated GO. ¹⁶

The oxidation states and surface chemical compositions of the as-prepared products were analyzed by X-ray photoelectron spectroscopy (XPS).⁵ Fig. S3A (ESI) displays the dominant XPS peaks emerged at 72.13, 286.08, 400.19, 532.23, and 854.98 eV, which are originated from Pt, Ni, C, N, and O elements in the survey spectrum, respectively.

For the high-resolution C 1s XPS spectrum (Fig. S3B, ESI), there are four peaks detected at 284.78, 286.22, 288.40, and 289.36 eV, matching well with the C–C, C–O, C=O, and O-C=O bonds, ¹⁶ respectively. The C-C (sp²) groups are assigned to the graphitic structure, ³⁰ which is the predominant species in Ni@PtNi NCs-rGO. The results indicate a significant loss of oxygen-containing functional groups and the formation of rGO, ³¹ which agrees well with Raman data (Fig. 3B).

As shown in Fig. S3C (ESI), the XPS spectrum of Pt 4f can be deconvoluted into two doublets. The stronger couple arising from metallic metallic Pt⁰ is observed at about 71.22 and 74.59 eV,³² while the other pair shows up at 72.41 eV and 76.42 eV which is assigned to Pt²⁺ in PtO or Pt(OH)₂.³³ By measuring the peak intensities of Pt⁰ and Pt²⁺, it clearly reveals that metallic

ARTICLE Journal Name

Pt⁰ is the evidently main species in Ni@PtNi NCs. Meanwhile, there is a different degree of up-shift for the peak positions as compared with pure metallic Pt, owing to the electron donation from Ni to Pt. ¹¹

As shown in Fig. S3D (ESI), the high binding energy near main peaks of Ni 2p displays remarkably high signal intensities, which is mainly originated from multi-electron excitation. 34,35 After taking the "shake-up" peaks into consideration, the peaks located at 852.76 (Ni 2p3/2) and 869.84 eV (Ni 2p1/2) correspond well with metallic Ni⁰,36 whereas the other ones at 856.16 and 874.42 eV are indexed to Ni²⁺ such as Ni(OH)₂ and/or NiO.³⁷ By comparing the related peak intensities, it is found that both Ni⁰ and Ni²⁺ are as the major species on the surface of Ni@PtNi NCs. These results are similar to the characteristic of PtNi bimetallic nanomaterials in the literature.³⁷

TGA analysis reveals good thermal stability of Ni@PtNi NCsrGO (Fig. S4, ESI). For each sample, the initial weight loss under 200 °C is equivalent to the physical water evaporation, whereas the loss at 200 - 800 °C is ascribed to the removal of oxygenated functional groups and the burning of the carbon skeleton. In protantly, Ni@PtNi NCs-rGO (curve a) displays small weight drops as compared to pure GO (curve b) under the same conditions. These observations prove the effective reduction of oxygen containing groups in graphene, further exhibiting the efficient reduction of GO after the solvothermal process. Furthermore, the metallic content in Ni@PtNi NCs-rGO is about 35 wt%.

The magnetic properties of the as-prepared Ni@PtNi NCs-rGO were measured at room temperature (300 K). As shown in Fig. 4, the sample exhibits no significant magnetic hysteresis, indicating the good soft-magnetic properties of Ni@PtNi NCs-rGO. Inset in Fig. 4 reveals the magnetic hysteresis loop at a lower field, demonstrating that the remnant magnetization (Mr) is very small (0.07 emu g $^{-1}$). This implies that the asprepared products exhibit nearly no magnetic properties without an external magnetic field.

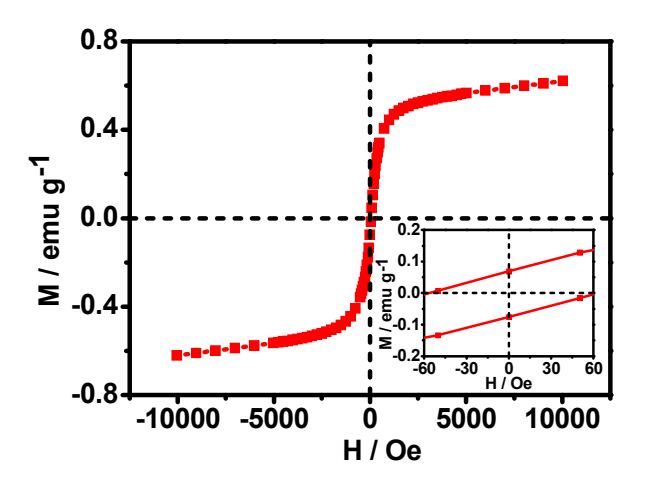


Fig. 4 Magnetic hysteresis loop of Ni@PtNi NCs-rGO measured at 300 K. Inset shows the magnetic hysteresis loop at a lower field.

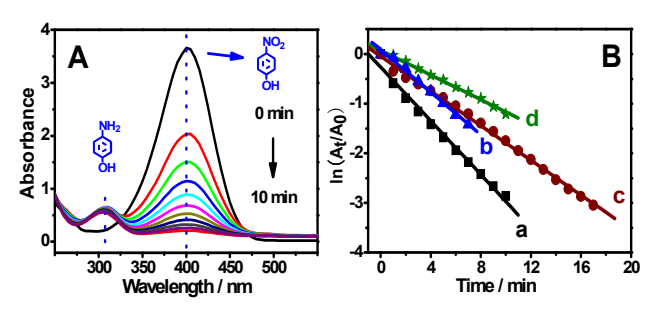


Fig. 5 (A) Time-dependent UV-vis spectra of p-NP reduction catalyzed by Ni@PtNi NCs-rGO with the concentration of 0.02 g L-1. (B) The plots of ln(At/A0) vs. reaction time toward p-NP reduction catalyzed by Ni@PtNi NCs-rGO (curve a), 50 wt% commercial Pt/C (curve b), Pt NPs/rGO (curve c), and Ni NPs/rGO (curve d), respectively.

3.2 Catalytic measurements

Fig. 5A illustrates the UV-vis absorption spectra of p-NP during the reaction process using Ni@PtNi NCs-rGO (0.02 g L⁻¹) as a catalyst. It can be seen that the maximum absorption peak appeared at 400 nm gradually declines as the reduction time proceeds, along with the gradual emergence of the new peak at 300 nm by extending the reaction time. Within 10 min, p-NP was completely reduced to p-aminophenol (p-AP). Fig. 6 indicates the possible catalytic mechanism of p-NP using Ni@PtNi NCs-rGO as a catalyst.

By contrast, the photocatalytic properties of commercial Pt/C (50 wt%), Pt NPs-rGO and Ni NPs-rGO were studied as referenced catalysts (Fig. 5B and Fig. S5, ESI). And the pseudofirst-order kinetics were employed to estimate the rate constants for p-NP reduction with excess NaBH4.38 The concentrations of p-NP at time t and 0 are defined as C_t and C₀, respectively. The relative peak intensity of the absorbance (A_t/A_0) is used to calculate the C_t/C_0 . As shown in Fig. 5B, $ln(A_t/A_0)$ shows linear responses with the reaction time for the reduction catalyzed by Ni@PtNi NCs-rGO (curve a), commercial Pt/C (curve b), Pt NPs-rGO (curve c), and Ni NPsrGO (curve d). All of the plots match well with the first-order reaction kinetics.³⁹ Specifically, the kinetic rate constant (k) is 4.5×10⁻³ s⁻¹ for Ni@PtNi NCs-rGO, which is larger than those of commercial Pt/C $(3.6 \times 10^{-3} \text{ s}^{-1})$, Pt NPs-rGO $(2.9 \times 10^{-3} \text{ s}^{-1})$, and Ni NPs-rGO $(2.1\times10^{-3} \text{ s}^{-1})$, indicating the enhanced catalytic activity of Ni@PtNi NCs-rGO.

With the purpose of comparing the catalytic activity of the as-synthesized catalyst with the others in the literature, the normalized rate constant (k_{nor}) was calculated based on the equation: $k_{nor} = k/m$, where m is the weight of the catalyst. According to the TGA analysis, Pt and Ni loadings were 35 wt% in Ni@PtNi NCs-rGO (Fig. S4, ESI). The k_{nor} value of Ni@PtNi NCs-rGO (257 s⁻¹ g⁻¹) is much higher than those previously reported, such as Ag@Au ($k_{nor} = 53.6 \text{ s}^{-1} \text{ g}^{-1}$), ⁴² Au/graphene ($k_{nor} = 31.7 \text{ s}^{-1} \text{ g}^{-1}$), ⁴¹ Au-Pd/CS ($k_{nor} = 14.6 \text{ s}^{-1} \text{ g}^{-1}$), ⁴² and Pd-Ag NPs ($k_{nor} = 8.3 \text{ s}^{-1} \text{ g}^{-1}$). ⁴³ All of the above observations further indicate the remarkable catalytic performance of Ni@PtNi NCs-rGO. This is attributed to the increased surface area of Ni@PtNi NCs-rGO (13.64 m² g⁻¹), as determined by Brunauer–Emmett–Teller measurement (Fig. 7). The apparent activation energy (E_a) is a vital parameter of a catalyst, which can be

Journal Name ARTICLE

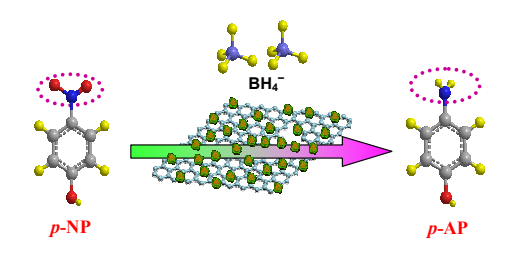


Fig. 6 Schematic illustration of the reduction of p-NP to p-AP over Ni@PtNi NCsrGO.

applied to evaluate its catalytic performance.⁴⁴ Thus, the catalytic reaction of p-NP was performed at 298 K, 308 K, 318 K, and 328 K (Fig. 8A and Fig. S6, ESI). As observed in Fig. 8A, the reaction rate is increased when the temperature increases. Table S1 (ESI) provides the k for the catalytic reactions of p-NP.

The apparent activation energy was calculated by the Arrhenius equation. ⁴⁵ The E_a of Ni@PtNi NCs-rGO is determined to be 6.97 kJ mol⁻¹ according to the Arrhenius plot of lnk against 1/T (Fig. 8B, curve a). This value is lower than those of the other nanocatalysts such as Au nanocages (28 kJ mol⁻¹), ⁴⁴ Ag/Fe₂O₃ microcubes (22.5 kJ mol⁻¹), ⁴⁶ and citrate-stabilized Au nanoparticles (31 kJ mol⁻¹). ⁴⁷ These results demonstrate that the reduction catalyzed by Ni@PtNi NCs-rGO possess a lower potential barrier and the reaction occurred via surface catalysis. ⁴⁶

According to Eyring equation, we can calculate thermophysical parameters such as activation entropy change ($\Delta S^{\#}$) and activation enthalpy change ($\Delta H^{\#}$). The $\Delta S^{\#}$ and $\Delta H^{\#}$ were estimated based on the plot of ln(k/T) against 1/T, as displayed in Fig. 8B (curve b). Table S1 (ESI) lists the associated $\Delta S^{\#}$ and $\Delta H^{\#}$ for p-NP reduction. When the catalytic reduction goes on, the negative entropy value indicates the gradually decreased randomness on the boundary of the catalyst and liquid.

The stability of Ni@PtNi NCs-rGO was investigated by recycling test in p-NP under the same conditions (Fig. 9 and Fig. S7, ESI). After one cycle of catalytic reaction completed, the catalyst was centrifuged and then washed with water b e f o r e i t

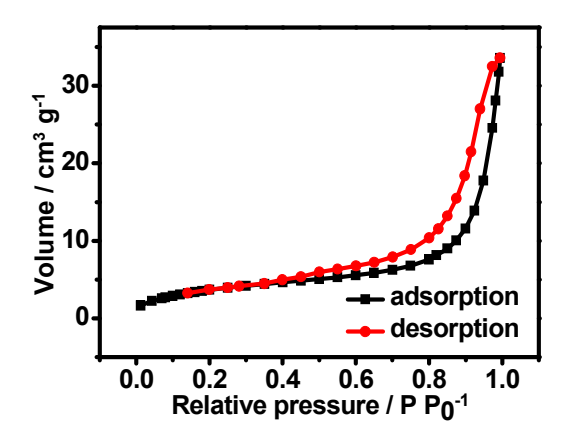


Fig. 7 Nitrogen adsorption/desorption analysis of Ni@PtNi NCs-rGO.

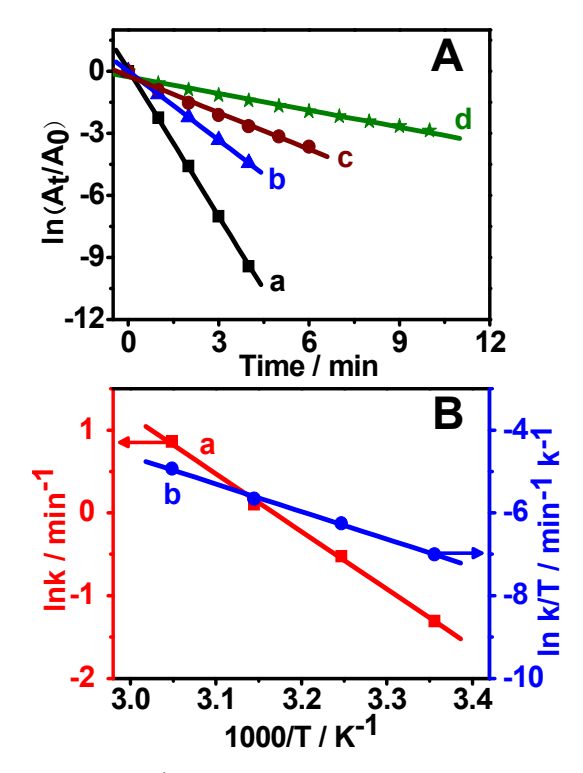


Fig. 8 (A) Plots of $\ln(At/A0)$ vs. reaction time for the catalytic reduction of p-NP at 328 K (curve a), 318 K (curve b), 308 K (curve c), and 298 K (curve d), respectively; (B) Plots of lnk vs. 1000/T for the estimation of the associated activation energy (curve a), Plots of $\ln(k/T)$ vs. 1000/T for the estimation of activation entropy change (curve b).

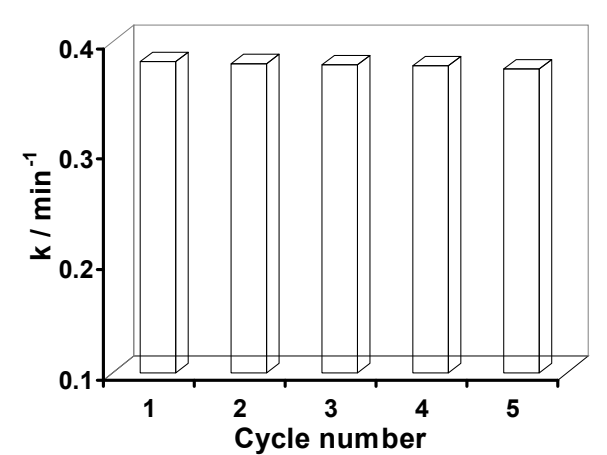


Fig. 9 The catalytic performance of five successive reduction reactions with 0.02 g $\rm L^{-1}$ Ni@PtNi NCs-rGO.

was reused for the next cycle. As seen in Fig. 9, Ni@PtNi NCs-rGO remains ca. 98.2% of their original catalytic efficiency after five cycles, indicating the superior stability of the catalyst against poisoning by the product of the reaction. The enhanced catalytic activity and improved stability of Ni@PtNi NCs-rGO are ascribed to the synergistic effects between Pt and Ni, 48 the improved electronic transport by using rGO as

ARTICLE Journal Name

support,⁵ along with unique yolk-shell nanostructures of 16 S. Stankovich, D. A. Dikin, R. D. Piner, K. A. Kohlhaas, A. Ni@PtNi NCs which provide more active sites available.

4. Conclusion

In summary, rGO supported well-defined yolk-shell Ni@PtNi NCs were manufactured by a facile one-step solvothermal method. The resultant Ni@PtNi NCs-rGO shows improved catalytic activity and stability for the reduction of p-NP to p-AP, compared with commercial Pt/C (50 wt%), monometallic Pt NPs-rGO, and Ni NPs-rGO, which might be mainly due to the unique volk-shell structure and synergistic effects between Pt and Ni. The yolk-shell nanostructure provides high specific surface area and more active sites available for the transport of medium molecules and electrons. The activation energy values confirm that the catalytic reactions occur via surface catalysis. The as-synthesized Ni@PtNi NCs-rGO can be served as an ideal photocatalyst in sewage treatment because of its increased catalytic efficiency for degradation of p-NP.

Acknowledgement

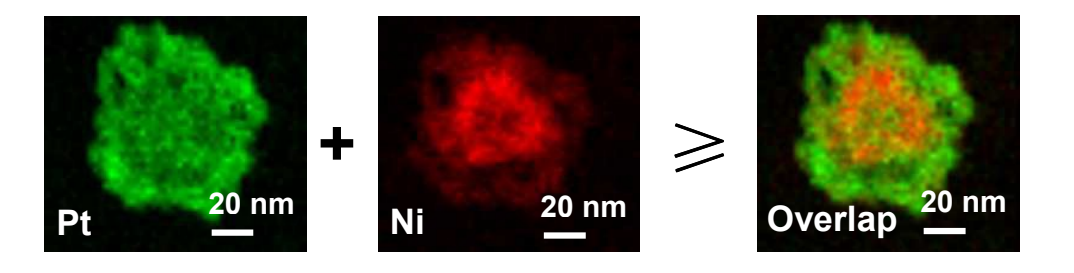
This work was financially supported by the National Natural Science Foundation of China (Nos. 21475118, 21175118, 21275130 and 21275131).

Notes and references

- 1 H. Hu, J. H. Xin, H. Hu, X. Wang, D. Miao and Y. Liu, J. Mater. Chem. A, 2015, 3, 11157.
- 2 X. Zhou, H. Li, H. Xiao, L. Li, Q. Zhao, T. Yang, J. Zuo and W. Huang, Dalton Trans., 2013, 42, 5718.
- 3 Z. Jiang, J. Xie, D. Jiang, X. Wei and M. Chen, Cryst. Eng. Comm, 2013, 15, 560.
- 4 P. Zhang, Y. Sui, G. Xiao, Y. Wang, C. Wang, B. Liu, G. Zou and B. Zou, J. Mater. Chem. A, 2013, 1, 1632.
- 5 P. K. Sahoo, B. Panigrahy and D. Bahadur, RSC Adv., 2014, 4, 48563.
- S. Gu, S. Wunder, Y. Lu, M. Ballauff, R. Fenger, K. Rademann, B. Jaquet and A. Zaccone, J. Phys. Chem. C, 2014, 118, 18618.
- Z. D. Pozun, S. E. Rodenbusch, E. Keller, K. Tran, W. Tang, K. J. Stevenson and G. Henkelman, J. Phys. Chem. C, 2013, 117, 7598.
- Y. Park, Y. W. Lee, S. W. Kang and S. W. Han, Nanoscale, 2014. **6**. 9798.
- 9 A. Habrioux, E. Sibert, K. Servat, W. Vogel, K. B. Kokoh and N. Alonso-Vante, J. Phys. Chem. B, 2007, 111, 10329.
- 10 Y. Hu, H. Zhang, P. Wu, H. Zhang, B. Zhou and C. Cai, Phys. Chem. Chem. Phys., 2011, 13, 4083.
- 11 X.-J. Liu, C.-H. Cui, M. Gong, H.-H. Li, Y. Xue, F.-J. Fan and S.-H. Yu, Chem. Commun., 2013, 49, 8704.
- 12 J. Zhang, K. Sasaki, E. Sutter and R. R. Adzic, Science, 2007,
- 13 S. J. Bae, S. J. Yoo, Y. Lim, S. Kim, Y. Lim, J. Choi, K. S. Nahm, S. J. Hwang, T.-H. Lim, S.-K. Kim and P. Kim, J. Mater. Chem., 2012, 22, 8820.
- 14 L. Liu, E. Pippel, R. Scholz and U. Gösele, Nano Lett., 2009, 9,
- 15 J. Wang, G. Yin, H. Liu, R. Li, R. L. Flemming and X. Sun, J. Power Sources, 2009, 194, 668.

- Kleinhammes, Y. Jia, Y. Wu, S. T. Nguyen and R. S. Ruoff, Carbon, 2007, 45, 1558.
- 17 Z. Zhang, F. Xiao, Y. Guo, S. Wang and Y. Liu, ACS Appl. Mat. Interfaces, 2013, 5, 2227.
- 18 S. Guo, S. Dong and E. Wang, ACS Nano, 2010, 4, 547.
- 19 L. Kuai, S. Wang and B. Geng, Chem. Commun., 2011, 47, 6093.
- 20 W. S. Hummers Jr and R. E. Offeman, J. Am. Chem. Soc., 1958, 80, 1339.
- 21 L.-P. Mei, P. Song, J.-J. Feng, J.-H. Shen, W. Wang, A.-J. Wang and X. Weng, Microchim. Acta, 2015, 182, 1701.
- 22 L. Wang and Y. Yamauchi, J. Am. Chem. Soc., 2013, 135, 16762.
- 23 B. M. Leonard, Q. Zhou, D. Wu and F. J. DiSalvo, Chem. Mater., 2011, 23, 1136.
- 24 S. Lee, H. J. Kim, S. M. Choi, M. H. Seo and W. B. Kim, Appl. Catal., A, 2012, 429-430, 39.
- 25 K. A. Kuttiyiel, K. Sasaki, Y. Choi, D. Su, P. Liu and R. R. Adzic, Nano Lett., 2012, 12, 6266.
- 26 D. Wang, Y. Li, Adv. Mater., 2011, 23, 1044.
- 27 W. Chen, L. Yan and P. R. Bangal, Carbon, 2010, 48, 1146.
- 28 S.-S. Li, J.-N. Zheng, X. Ma, Y.-Y. Hu, A.-J. Wang, J.-R. Chen and J.-J. Feng, Nanoscale, 2014, 6, 5708.
- 29 S.-S. Li, J.-J. Lv, Y.-Y. Hu, J.-N. Zheng, J.-R. Chen, A.-J. Wang and J.-J. Feng, J. Power Sources, 2014, 247, 213.
- 30 J. Y. Park and S. Kim, Int. J. Hydrogen Energy, 2013, 38, 6275.
- 31 Y. Chen, X. Zhang, D. Zhang, P. Yu and Y. Ma, Carbon, 2011, **49**. 573.
- 32 L. Nie, J. Yu, X. Li, B. Cheng, G. Liu and M. Jaroniec, Environ. Sci. Technol., 2013, 47, 2777.
- 33 F. Liu, J. Y. Lee and W. J. Zhou, Small, 2006, 2, 121.
- 34 R. Schulz, A. Van Neste, P. Zielinski, S. Boily, F. Czerwinski, J. Szpunar and S. Kaliaguine, Catal. Lett., 1995, 35, 89.
- 35 I. G. Casella, M. R. Guascito and M. G. Sannazzaro, J. Electroanal. Chem., 1999, 462, 202.
- 36 Y. Hu, P. Wu, Y. Yin, H. Zhang and C. Cai, Appl. Catal., B, 2012, 111-112, 208.
- 37 K.-W. Park, J.-H. Choi, B.-K. Kwon, S.-A. Lee, Y.-E. Sung, H.-Y. Ha, S.-A. Hong, H. Kim and A. Wieckowski, J. Phys. Chem. B, 2002, **106**, 1869.
- 38 K.-L. Wu, X.-W. Wei, X.-M. Zhou, D.-H. Wu, X.-W. Liu, Y. Ye and Q. Wang, J. Phys. Chem. C, 2011, 115, 16268.
- 39 F. Ke, J. Zhu, L.-G. Qiu and X. Jiang, Chem. Commun., 2013, 49, 1267.
- 40 C.-H. Liu, X.-Q. Chen, Y.-F. Hu, T.-K. Sham, Q.-J. Sun, J.-B. Chang, X. Gao, X.-H. Sun and S.-D. Wang, ACS Appl. Mat. Interfaces, 2013, 5, 5072.
- 41 J. Li, C.-y. Liu and Y. Liu, J. Mater. Chem., 2012, 22, 8426.
- 42 S. Tang, S. Vongehr, G. He, L. Chen and X. Meng, J. Colloid Interface Sci., 2012, 375, 125.
- 43 J. Huang, S. Vongehr, S. Tang, H. Lu and X. Meng, J. Phys. Chem. C, 2010, 114, 15005.
- 44 H. Li, J. Liao and Z. Xibin, J. Mater. Chem. A, 2014, 2, 17530.
- 45 V. K. Gupta, N. Atar, M. L. Yola, Z. Üstündağ and L. Uzun, Water Res., 2014, 48, 210.
- 46 Z. Jiang, D. Jiang, A. M. Showkot Hossain, K. Qian and J. Xie, Phys. Chem. Chem. Phys., 2015, 17, 2550.
- 47 S. Panigrahi, S. Basu, S. Praharaj, S. Pande, S. Jana, A. Pal, S. K. Ghosh and T. Pal, J. Phys. Chem. C, 2007, 111, 4596.
- 48 R. Liu, Q. Zhao, Y. Li, G. Zhang, F. Zhang and X. Fan, J. Nanomater., 2013, 2013, 1.

Graphical Abstract



Bimetallic yolk-shell Ni@PtNi NCs-rGO were facilely prepared by a one-pot solvothermal method, which exhibited enhanced catalytic performance for *p*-nitrophenol reduction.